Porosity of metamorphic rocks and fluid migration within subduction interfaces

Anne-Céline Ganzhorn, Hélène Pilorgé, Bruno Reynard

Porosity of metamorphic rocks and fluid migration within subduction interfaces

A.C. Ganzhorn[1], H. Pilorgé[1], B. Reynard[1*]

[1] University of Lyon, ENS de Lyon, Université Claude Bernard Lyon 1, CNRS, UMR 5276 LGL-TPE*, 46 Allée d'Italie, F-69007 Lyon, France

*Corresponding author: bruno.reynard@ens-lyon.fr

Abstract:

Large earthquakes break the subduction interface to depths of 60 to 80 km. Current models hold that seismic rupture occurs when fluid overpressure builds in link with porosity cycles, an assumption still to be experimentally validated at high pressures. Porosities of subduction zone rocks are experimentally determined under pressures equivalent to depths of up to 90 km with a novel experimental approach that uses Raman deuterium-hydrogen mapping. Natural rocks (blueschists, antigorite serpentinites, and chlorite-schists) representing a typical cross-section of the subduction interface corresponding to the deep seismogenic zone are investigated. In serpentinite, and to a smaller extent blueschist, porosity increases with deformation, whereas chlorite-rich schists remain impermeable regardless of their deformation history. Such a contrasting behavior explains the observation of over-pressurized oceanic crust and the limited hydration of the forearc mantle wedge. These results provide quantitative evidence that serpentinite, and likely blueschist, may undergo porosity cycles making possible the downdip propagation of large seismic rupture to great depths.

Keywords: subduction interface, porosity, permeability, seismic cycle, fluid overpressure

1. Introduction

The interface between a subducting oceanic plate and overriding lithosphere and mantle wedge (the subduction interface) is an area of intense seismic activity. Models of the earthquake cycle have invoked fluid pressure variations to explain faulting behavior. Fluid pressure progressively increases to near lithostatic values during the inter-seismic period before it is released during an earthquake rupture (Sleep and Blanpied, 1992). Fluid pressure variations may be explained either by upward fluid movement through a rigid matrix or by compaction of the deformable fault zone (Sleep and Blanpied, 1992), both associated with permeability changes. The seismic cycle is associated with a “porosity” cycle, with porosity decreasing during the inter-seismic phase, and increasing through brittle deformation during an earthquake. Porosity and permeability are also fundamental parameters in modeling of fluid circulation, and its influence on frictional behavior (Khoshmanesh and Shirzai, 2018).

Permeability and fluid pressure variations during the seismic cycle have been confirmed by in-situ measurements of heat flow and residual temperature on the subduction interface (Fulton et al., 2013). Variations of the hydrological properties of crustal rocks between seismic and interseismic periods is also inferred from hydraulic measurements (Ingebritsen and Manning, 2010). Fluid overpressures in the subducted oceanic crust are imaged by seismology (Audet et al., 2009; Shiina et al., 2013), and require contrasted hydrological properties in the different lithologies of the oceanic crust and overlying mantle (Peacock et al., 2011). Porosity and permeability are also essential for modeling fluid flow in the various lithological layers dipping along the megathrust interface (Morishige and van Keken, 2018).

Experimental values of rock porosity and permeability need to be determined as critical parameters for numerical simulations of subduction dynamics (Audet et al., 2009;

Peacock et al., 2011). Direct porosity or permeability measurements based on fluid flow measurements are restricted to confining pressures up to 150 MPa (Katayama et al., 2012; Kawano et al., 2011; Shmonov et al., 1995), a pressure range that addresses the upper five kilometers of the seismogenic zone, where clay minerals dominate the interface (Chester et al., 2013; Ujiie et al., 2013). Extrapolation to greater depths is uncertain. Use of the Kozeny-Carman relationship on ambient temperature experiments in the 50-100 MPa range (Katayama et al., 2012; Kawano et al., 2011) yields permeabilities below 10^{-21} m^2 at subduction zone pressures, a threshold below which rocks are impermeable. Similar experiments up to 150 MPa (Shmonov et al., 1995) indicate stabilization of the permeability values in the 100-150 MPa range instead of a continuous decrease with increasing pressure, and a complex behavior upon heating and reaching dehydration of hydrated rocks around 300-400°C for serpentines.

At higher temperatures, permeability and fluid connectivity have been determined under conditions (800 - 1200°C, 1 - 5 GPa) pertinent to magmas under volcanic arcs, and where minerals can reach textural equilibrium with fluids (Mibe et al., 1999; Wark and Watson, 1998). These textural equilibrium experiments may capture the long-term behavior of polycrystalline aggregates with dry minerals of moderate anisotropy (olivine, quartz) but they are not relevant to highly anisotropic materials such as amphiboles and phyllosilicates stable in forearc rocks, and at high deformation rates.

In order to bridge the gap between the low- and high-pressure high-temperature range, we developed a novel experimental technique that uses Raman deuterium-hydrogen mapping to determine the porosity of metamorphic rocks (blueschists, antigorite serpentinites, and chlorite-schists) representing a typical cross-section of the subduction interface corresponding to the deep seismogenic zone. They represent, respectively, the metamorphosed oceanic crust at the footwall of the subduction megathrust, the hydrated forearc mantle wedge at the

hanging wall, and the metasomatic rocks or sediments at the interface between the subducting plate and the mantle wedge (Spandler et al., 2008). Experiments were conducted up to 3 GPa corresponding to depths of about 90 km. This covers the portion of the subduction interface that requires mechanical decoupling for matching the heat flux observations in geodynamic thermal models (Syracuse et al., 2010; Wada et al., 2008).

2. Methods

2.1 Starting material

We used four different natural rocks, all dominated by one or two hydrated mineral: two serpentinites (SB: BCS16a from Baja California, Mexico, and SC: Cu12 from Escambray Massif, Central Cuba) dominated by antigorite, one chlorite-schist (C: SZ24 from the Saas-Zermatt unit, Western Alps) dominated by chlorite, and one blueschist (G: from Groix Island, French Armorican Massif) dominated by glaucophane and epidote. These rocks are representative of high-pressure low-temperature fossil subduction rocks, i.e. with mineral assemblages, compositions, and strength corresponding to subduction zones.

The two serpentinites are dominated by antigorite, the high-temperature form of serpentine (Schwartz et al., 2013), with minor amount of chlorite, magnetite and carbonate (less than 5% in both rocks). SC also contains traces (<5% each) of lizardite and chrysotile, the two other varieties of serpentine. Chemical formulas for the m = 14 modulation of antigorite are $(Mg_{2.52}Fe_{0.24}Al_{0.01})_{\Sigma=2.77}(Al_{0.06}Si_{1.94})_{\Sigma=2}O_5(OH)_{3.57}$ for SB (Pilorgé et al., 2017), and $(Mg_{2.54}Fe_{0.16}Cr_{0.01}Al_{0.09})_{\Sigma=2.8}(Al_{0.1}Si_{1.9})_{\Sigma=2}O_5(OH)_{3.7}$ for SC (Reynard et al., 2011). Antigorite grains are up to 100-150 µm long and 10-20 µm-thick, with grain size being slightly lower in SB than in SC. SB is heterogeneously deformed and exhibits narrow zones of low-temperature semi-brittle deformation surrounding zones with high-temperature

schistosity. We refer to it as the deformed serpentinite. SC has a high-temperature schistosity of strong to very strong intensity (Bezacier et al., 2010) with well-recrystallized individual grains and does not exhibit significant retrograde deformation. We refer to it as the undeformed serpentinite.

The chlorite-schist (C) is composed mainly of chlorite (>95%) with minor magnetite and carbonate (<5%). The chemical formula of chlorite grains (100-500 µm-long and 10-50 µm-thick) is $(Mg_{8.93}Fe^{2+}_{0.16}\square_{0.18},Al_{1.98})(Si_{6.37}Al_{1.63})O_{20}OH_{16}$ (Ganzhorn et al., 2018). They are well recrystallized and almost free of deformation.

The blueschist (G) exhibits a mineralogical foliation with glaucophane-rich layers (600-1000 µm thick) alternating with epidote-rich layers (200-1000 µm thick). The glaucophane-rich layers were selected for experiments. They mainly contain glaucophane (>95%) with minor epidote, quartz, garnet, and titanite (<5%). Chemical formulas are $Na_{1.8}Ca_{0.2}Fe_{1.0}Mg_{2.28}Al_{1.9}Si_{7.7}O_{22}(OH)_2$ for glaucophane and $Ca_{1.9}Al_{2.5}Fe_{0.5}Si_3O_{12}(OH)$ for epidote. Glaucophane and epidote grains are ca. 30 µm long. Grains are well recrystallized and show little evidence of internal deformation in the form of subgrain boundaries.

The same preparation protocol was applied to all natural rocks. Hand-scale sample was crushed separately in an agate mortar and the different fractions were separated by a series of sieves. Two different grain sizes of powder were used for experiments on serpentinite (<125-100> µm sieves and <50 µm sieve) and only a single grain size was used for the other natural rocks (<125-100> µm sieves for chlorite-schist and <80 µm sieve for blueschist). Two grain-sizes of powder were used in the first experiments in order to test for compaction, water fraction and kinetic effects, after which the largest grain size of powder was preferred. This allowed increasing the amount of initial deuterated water from 3-10 wt% to 10-20 wt%. Sub-micrometric particles were left in the fraction as they dissolve more

readily in water during the high-temperature stage, saturating the fluid so that it is in equilibrium with the rock, limiting as far as possible potential dissolution within it.

Intact rock pieces were introduced in the experimental charge along with powder to simulate pristine rocks (Fig. 1). When possible, cores of about 1.5 mm diameter were used. When it was not possible to core the rock due to schistosity and brittle behavior, chips of several hundreds of micrometers were used.

2.2. High-pressure experiments

Experiments were performed in a belt apparatus at the University of Lyon 1 (Fig. 1). The belt press is a high-volume press with typical sample size of 70 mm^3. The powders and one core, or one to three chips of natural rocks were loaded in a gold capsule (6 mm-long and 4 mm in diameter). Powders were soaked with D_2O (purity 99 atom%, Sigma-Aldrich) that filled the porosity.

Capsules are designed to seal in the belt apparatus while pressure is increased at ambient temperature (Pilorgé et al., 2017). In order to limit D_2O leakage at ambient pressure and temperature, D_2O was added and capsules were closed only a few hours (3-5) before running experiments. Additionally, they were wrapped in paraffin film and kept frozen until used in the belt apparatus. Experiment names, *e.g.* C-XX-315, are built as follow: the first letter indicates the protolith (SB: serpentinite BSC16a, SC: serpentinite Cu12, C: chlorite-schist, G: glaucophane-rich blueschist), XX is the number of the experiment, and the last number indicates the experimental temperature of isotopic exchange.

Belt experiments were run at several temperatures and 1.5 - 3 GPa for 12 - 38 hours. Each gold capsule was placed in an insulating boron nitride gasket inside a cylindrical graphite furnace which itself was surrounded by a pyrophyllite gasket. Pressure was calibrated against the room temperature fixed-point metal transitions and the high-temperature

quartz to coesite transition. Due to the design of the belt press, temperature cannot be directly monitored with a thermocouple but is calculated from the calibrated relationship between input power and capsule temperature. Input power – capsule temperature was calibrated at 1 and 5 GPa over a broad range of temperatures (25-1000°C), and temperature uncertainty is estimated to be ±40°C (Koga et al., 2005).

The sample was pressurized at room temperature before heating (Fig. 1) for 12 to 48 hours at constant pressure and temperature, the only stage at which isotopic exchange between fluids and minerals is possible through diffusion. Samples were then quenched to ambient temperature before decreasing the pressure within a few hours (0.02 GPa/min). Recovered capsules were deformed with a shape ratio (length/diameter) ca. 0.5 to be compared with the initial ratio of 1.4. Deformation occurred due to the soft pressure media (i.e. the boron nitride) and the high D_2O content and high porosity of the powder.

The weight of deformed capsules was monitored before and after piercing and drying at 120°C for 10 minutes in a sterilizer. Weight loss after drying indicates that capsules still contained water after the experiments. It was demonstrated that with this type of capsule and assemblage, the loss of D_2O during an experiment and the hydrogen loss and water dissociation were low (Ganzhorn et al., 2018; Pilorgé et al., 2017). Thus capsules are assumed to be closed systems.

Quenched capsules were mounted in epoxy resin and cut lengthwise in two parts with a wire diamond saw. Both parts were then entirely remounted in epoxy to properly fix the loose crystals in the powder. They were polished with silicon carbide abrasive paper down to a grain size of 2.5 µm, and then with a solution of alumina down to 0.5 µm. Cores (or chips) were sometimes lost during the preparation due to poor mechanical integrity of the powder.

2.3. Raman spectroscopy

We used a Horiba™ LabRam HR Evolution and a 532 nm continuous wave laser source. This confocal setup coupled with an objective of x100 magnification and a high-resolution stage for the sample movements allowed us to acquire hyperspectral images with spatial resolutions between 0.5 to 1.5 µm depending on the map size. Each spectrum was acquired in 2 accumulations of 2 seconds with a laser power of 30 mW on the sample.

No deuterium was detected in the characteristic Raman spectra of the hydrous mineral of the studied natural rocks, owing to the low natural deuterium abundance (< 0.02 atom%), well below the detection limit ca. 0.1% at most. OD vibrations are observed only after interaction with D_2O at high pressure and temperature. For all investigated minerals, OD and OH bonds have different Raman shifts in the regions 2440 - 2745 cm^{-1} and 3300 - 3720 cm^{-1}, respectively, allowing good discrimination between the two. Epidote has the lowest Raman shifts (2440 - 2560, 3301 - 3426 cm^{-1}), glaucophane shows thin bands (2671 - 2712, 3613 - 3674 cm^{-1}), antigorite has several bands in the 2600-2730 and 3560-3700 cm^{-1} range, and chlorite shows the broadest bands (2460 - 2730, 3310 - 3700 cm^{-1}).

For each mineral, the OD bands are strictly homologous to the OH bands with a frequency ratio of 1.356±0.001, which correspond to the theoretical harmonic reduced mass ratio (1.374) and to minor anharmonic effects (Reynard and Caracas, 2009). This indicates that deuterium substitutes for hydrogen on their crystallographic sites through a lattice diffusion process without modifications of the mineral chemistry or structure, and that dissolution and precipitation processes, if any, are not detected by Raman or observed by SEM. By integrating the area below OD and OH bands, it is possible to calculate the D/(D+H) ratio for each spectrum and convert the Raman map into a D/(D+H) map (Ganzhorn et al., 2018; Pilorgé et al., 2017).

2.4. Quantification of porosity from D/(D+H) maps

The method of porosity quantification was designed to account for and take advantage of lattice diffusion. Because fluid is lost after the opening of the capsule, the only trace of fluid-mineral interactions is an increase of D/(D+H) ratio in the mineral with diffusion profiles starting from grain boundaries and smoothly decreasing towards the interior of the grains (Pilorgé et al., 2017). Typical diffusion patterns can be compared with actual grain boundaries and fractures from SEM observations (Fig. 2). In this example, a thin blade of antigorite that displays a continuous crystallographic orientation throughout the image displays two sectors affected by intra-crystalline deuterium diffusion. On close inspection by SEM (Fig. 2c), the limit between the two sectors shows nano-porosity that was as active fluid path during the high-temperature stage because diffusion occurred along it. Other cracks that are easily seen on SEM images crosscut the isotopic zoning and postdate it. They were likely formed during decompression of the sample. This shows that isotopic exchange is a much more pertinent tool to locate "active" porosity, i.e. open fluid paths, during the high-pressure high-temperature experiments than SEM image analysis. In the following, instead of using the isotopic profiles to obtain lattice diffusion coefficients, we use isotopic maps to infer active porosity during the high-pressure high-temperature stage of the experiment when deuterium-hydrogen exchange between the fluid and the rock occurs.

When diffusion coefficients are around 10^{-20} m^2/s, the distance over which lattice diffusion occurs is of the order of tens of nanometers, smaller than the Raman beam size (ca. 500 nm) used to map D/(D+H) ratios. In these conditions, deuterium-bearing zones observed in hydrated mineral on Raman maps are identified with locations of fluid-mineral interface at the time of experiments. D/(D+H) ratios are proportional to the active, i.e. fluid-filled, grain boundary density (Fig. 3). We then make the assumption that higher D/(D+H) ratios correspond to the creation of numerous new grain boundaries that are identified as cracks on SEM images of a serpentinite experiment (Fig. 4). Corrugated cracks or grain boundaries may

occur and could invalidate the assumption or straight boundaries made here because of overlapping diffusion profiles. This is not the case when diffusion length is small as in the present experiments with low diffusion coefficients. SEM images indicate little corrugation and tortuosity of grain boundaries. Zones with foliation orientation subperpendicular to the sample section are dominant because of shape orientation of the rock chip or core, ensuring that a majority of grain boundaries are subperpendicular to the studied sections.

Conversion of D/(D+H) ratios into grain boundary density per unit area is achieved by calculating synthetic D/(D+H) ratios corresponding to given numbers of grain boundaries (n) in one pixel (Fig. 3b). We then use the solution of the diffusion equation for a plane sheet in contact with an infinite reservoir, considering small time (i.e. duration of experiment is small in comparison to a characteristic diffusion time) from (Cranck, 1975), to calculate diffusion profile between two grain boundaries bounding a planar element of mineral (our plane sheet):

$$\frac{C(x)-C_0}{C_1-C_0} = \sum_{m=0}^{\infty}(-1)^m \mathrm{erfc}\left(\frac{(2m+1)l-x}{2\sqrt{Dt}}\right) + \sum_{m=0}^{\infty}(-1)^m \mathrm{erfc}\left(\frac{(2m+1)l+x}{2\sqrt{Dt}}\right) \quad (1),$$

with $C(x)$ the mineral D/(D+H) ratio at the position x, C_0 the initial mineral D/(D+H) (=0 in our case), C_1 the fluid D/(D+H) ratio at fluid-mineral interfaces (x=-l and x=l, i.e. at crack location, Fig. 3c), l the half thickness of the plate sheet (in m), D the diffusion coefficient (in m^2/s), and t the experiment duration (in s). This solution converges rapidly and the infinite sums may be approximated with the three first terms (m=0 to 3). The synthetic D/(D+H) ratio of one pixel for a known amount of grain boundary (n) is then:

$$\frac{\mathrm{D}}{\mathrm{D+H}} = \frac{2n}{Y}\int_{x=0}^{l} C(x)\,dx \qquad (2),$$

with Y the pixel size (in m) and $C(x)$ the D/(D+H) profile for a half space plane sheet calculated with equation (1) for m = 0 to 3. The integral was approximated with the trapeze method. We then calculate the evolution of D/(D+H) for one pixel with the number of grain boundary per unit length using equation (2) (Fig. 3d). This relationship was then fitted with a linear function over a restricted range of grain boundary number above which the chosen

249 solution to the diffusion equation is not valid anymore (*e.g.* the last two points in Fig. 3d).
250 Actual experimental values were such that this hypothesis is verified. A different function was
251 generated for each experiment taking into account the Raman map pixel size (Y), the
252 corresponding diffusion coefficient, experiment duration and average effective C_1 (Pilorgé et
253 al., 2017). Finally, D/(D+H) Raman maps are converted in grain boundary density maps using
254 the corresponding function (Fig. 3e).

255 2D porosity was calculated as the mean grain boundary density of the map multiplied
256 by the grain boundary thickness δl. δl is of the order of 0.4 nm in olivine aggregates (Hiraga
257 et al., 2004) with lattice parameters in the 0.5 - 0.8 nm range. The present minerals have more
258 complex structures, and this value is likely higher. Scaling δl with lattice parameters in the 0.5
259 - 4 nm range, we estimate δl in the 0.5 - 2 nm range, which is consistent with HRTEM images
260 of both naturally and experimentally deformed serpentine samples (Amiguet et al., 2014).

261 From experiments at various temperatures, the inter-diffusivity of deuterium-hydrogen
262 was determined in the different hydrous minerals. For antigorite and chlorite deuterium-
263 hydrogen inter-diffusivity is within the required range at 315°C ($10^{-20.6}$ and $10^{-20.7}$ m^2/s
264 respectively (Ganzhorn et al., 2018; Pilorgé et al., 2017). In the case of glaucophane,
265 deuterium-hydrogen inter-diffusivity at 315°C is so low that almost no incorporation of
266 deuterium is seen in glaucophane grains after high-pressure experiments. To overcome the
267 very slow diffusion in glaucophane, we set the temperature to 500°C (G-28-500) and 450°C
268 (G-31-450) where the diffusion coefficients for glaucophane of $10^{-18.7}$ and $10^{-20.3}$ m^2/s,
269 respectively, are estimated from preliminary room pressure exchange experiments between D_2
270 gas and glaucophane. Estimated uncertainties on diffusion coefficients are of one order of
271 magnitude and are taken into account in error propagation on porosity determination.

272 As a result, among some thirty experiments, only five (Table 1) could be selected
273 because they fall in the range where deuterium-hydrogen diffusion in minerals can be used to

estimate porosity in the rock core or chip, at temperatures of 315°C (experiments SB-4-315, SC-24-315, C-25-315) for chlorite- and antigorite-dominated rocks, and of 450-500°C (experiments G-28-500 and G-31-450) for the glaucophane-dominated rock. The good agreement between porosity determinations at 450 and 500°C for the blueschist (Table 1) with one and a half order of magnitude difference in diffusion coefficient validates the approach, although the explored temperature range is small due to constrains on diffusion coefficients and thermal stability of hydrated minerals.

3. Results

The present experiments simulate the deformation sequence of the seismic cycle in water-saturated rocks: a short and intense pulse of cold compression representing an initial earthquake is followed by a rest period with lower stress and slower deformation. Cores or chips and powder of selected rocks are enclosed in a gold capsule and loaded in a belt press (Fig. 1a). The first stage is a pressure and temperature increase (< 900 s) that models the deformation event, with 85±5% of the deformation occurring during it as recorded by piston displacement in the press (Fig. 1b). Associated strain rates are on the order of 10^{-3} s^{-1}, and most of the deformation is taken up by compaction and deformation of the water-saturated rock powder around rock cores or chips, which results in a large shape change of the gold capsule observed after the experiments (Fig. 1a). Stresses are high enough to induce deformation in the presence of excess water when rock cores are used. Texture and deformation heterogeneities were also inherited from those of the starting material in the case for thin rock chips embedded in rock powder. Deformation results in smallest grain sizes identified with optical microscopy or SEM.

The second stage corresponds to a pressure and temperature plateau during which the rocks interact with ambient aqueous solutions. With maximum strain rates of 10^{-5} s^{-1} during

this stage, stresses are constrained by plastic flow of boron nitride, the deformable material surrounding the capsule, to values below 10 MPa at 315°C, and to even lower values at 500°C (Pezzotti et al., 1997). These values are lower than the plastic or brittle yield stress of the minerals studied here. The second stage is a suitable representation of metamorphic conditions, and of the beginning of the inter-seismic relaxation period, during which samples exchanged hydrogen with deuterated water during the high-temperature plateau. Isotopic exchange is limited to the high-temperature stage because diffusion is negligible at ambient temperature.

Raman mapping of the isotopic exchange observed in the recovered samples is used to constrain porosity with deuterium-hydrogen inter-diffusivity in minerals close to 10^{-20} m^2/s. In these conditions (see above), Raman measurements of the D/(D+H) ratio are proportional to the density of grain boundaries that experienced fluid-rock interaction during the experiment, a method validated by comparison with SEM images (Fig. 4). D/(D+H) maps are converted to grain boundary densities, and then to 2D porosities by multiplying grain boundary density by grain-boundary thickness, which we assume to be in the 0.5 - 2 nanometer range (Amiguet et al., 2014; Hiraga et al., 2004). 2D porosities are converted in 3D porosities assuming a ratio close to unity for the platelet and elongated geometry of the phyllosilicates and inosilicates studied here.

The five studied samples show different intensities of fluid-rock exchange (Fig. 5), hence different porosities of 0.2 - 2.6×10^{-2} for the blueschist, 0.1 - 6×10^{-3} and 1 - 16×10^{-3} for serpentinite in the undeformed sample SC and deformed sample SB, respectively, and 1 - 19×10^{-4} for the chlorite-schist. In sample SB, deformation is heterogeneous, and deformed areas detected by SEM (P2 in Fig. 5b) displays higher porosities (4 - 16×10^{-3}) than undeformed areas (1 - 3×10^{-3}, P1 in Fig. 5b). The largest porosities of the deformed areas of the rock core are similar to the porosity of the deformed powder surrounding it (Fig. 6).

Values given above include uncertainties on pore width in the 0.5-2 nm range, and on diffusion coefficient of one order of magnitude (Table 1). Chlorite-schist retains low porosity even in the powdered part of the sample (Fig 5d). The blueschist chip shows measurable porosity heterogeneity associated with deformation heterogeneity in the starting material (0.2 - 1.0×10^{-2} *vs.* 0.6 - 2.6×10^{-2}, Fig. 6), although smaller than observed for serpentinite SB.

4. Discussion

Differences in mechanical properties of the major rock-forming mineral can explain the variety of porosity increase on deformation. Plastic yield stress exceeds 700 MPa in antigorite (Hilairet et al., 2007) because of corrugated structure that hinders basal slip (Amiguet et al., 2014), and 100 - 300 MPa in amphibole, *e.g.* glaucophane (Ko and Jung, 2015). In the presence of excess water, the yield stress of amphiboles drops down to about 60±20 MPa because brittle failure is favored (Ko and Jung, 2015). This typical brittle yield stress in the presence of excess water is commensurate with stresses expected at the subduction interface of a few tens of MPa (Fagereng and den Hartog, 2016). Chlorite yields plastically at similar stresses as micas, lizardite and talc, all phyllosilicates with easy slip on continuous basal plane planes (Amiguet et al., 2014), in the 20 - 100 MPa range (Amiguet et al., 2012; Kronenberg et al., 1990). Chlorite, micas, and talc, with their low plastic yield for basal slip, are the only class of mineral capable of deforming plastically in deep subduction zone conditions, therefore maintaining low porosity even for large strain and strain rates. Optical and SEM observations on the recovered samples confirm that chlorite shows extensive plastic deformation with smoothly bent crystals.

Porosities are similar in the undeformed serpentinite sample SC and in chlorite-schist, and increases by one order of magnitude in the deformed areas of serpentinite sample SB. The porosity difference between deformed serpentinite and chlorite-schist may be explained by

their different deformation mode. Bending and kinking of chlorite grains prevent the creation of new porosity and chlorite-schists remain impermeable during deformation. Likewise, low porosities are also expected for other phyllosilicates with continuous layers and low yield stress such as micas and talc (Amiguet et al., 2014). In contrast, deformation in antigorite or in glaucophane grains generates new grain boundaries, which act as open porosity, explaining the one order-of-magnitude difference in porosity between deformed and undeformed serpentinite (Fig. 6), and of half-an-order of magnitude in blueschists.

Porosities obtained in this study (Fig. 7) are similar to those of gabbro and serpentinite at 100 MPa (Katayama et al., 2012), and at least two orders of magnitude higher than extrapolated at 1 GPa by these authors from the trend of their low-pressure measurements. Present values of porosities are about one order of magnitude lower than those measured in textural equilibrium experiments on olivine or quartzite (Mibe et al., 1999; Wark and Watson, 1998). Once porosities are determined, permeabilities may be inferred from porosity values using the Kozeny-Carman relationship (Walder and Nur, 1984):

$$k = k_0 \left(\frac{\phi}{\phi_0}\right)^n \qquad (1),$$

where ϕ□□□ the porosity corresponding to the permeabilities *k,* with ϕ_0 and k_0 being reference values. The exponent n in equation (1) take different values depending on rock type and pore geometry. Values for reference porosity (ϕ_0=0.005) and permeability ($k_0=10^{-20.1}$) and n=2 were anchored on those from previous studies on similar rocks as those studied here (Katayama et al., 2012). Different values and exponent of n=3 are obtained in synthetic quartzite (Fig. 7a) because pores have well-equilibrated shapes at triple junctions and can be described by a wetting angle (Wark and Watson, 1998). This is not the case in the present study and in that of Katayama et al. (2012) where sharp and straight grain boundaries dominate due to the easy cleavage of minerals and low temperatures that do not allow textural

equilibration. Permeabilities are estimated in the 10^{-24} - 10^{-18} m^2 range (Fig. 7a), with uncertainties of the same order of magnitude as those obtained from modeling of fluid or heat flow in the continental crust (Ingebritsen and Manning, 1999; Ingebritsen and Manning, 2010) or from measurements on rock cores from deep drilling (Shmonov et al., 2003).

Rock permeabilities of subduction zone rocks from the present study can be compared with those of crustal rocks as a function of depth (Fig. 7b) in stable metamorphic conditions and after earthquakes (Ingebritsen and Manning, 1999; Ingebritsen and Manning, 2010; Shmonov et al., 2003). Values for blueschists fall within the trend for stable continental crust, and those for antigorite serpentinite SB and chlorite schist are lower than 10^{-21} m^2, indicating that these rocks are practically impermeable. Low permeabilities were also inferred from hydraulic studies in metamorphic terrains (Sanford, 2017). Values for highly deformed areas in serpentinite SB are similar to those of the blueschist, indicating that porosity and permeability increase by about one and two orders of magnitude, respectively, with deformation. This difference is similar to that inferred between stable continental crust rocks and fault zones after earthquakes (Ingebritsen and Manning, 2010), but absolute values are lower for serpentinites than for continental crust.

The present high-pressure determination of porosity and permeability offers a new perspective on the distribution of seismicity in subduction zones at forearc depths (35 - 90 km). Low frictional coefficient or high transient pore-fluid pressure required in order to generate earthquakes call for a control of seismic activity by a porosity cycle (Sleep and Blanpied, 1992) with porosity in the range of 1×10^{-3} - 1×10^{-2} depending on the model. The present determinations of porosity show that serpentinites experience the largest porosity variations with deformation compatible with the range for seismic rupture defined above. In blueschist, porosity variation is less pronounced, but sufficient to facilitate seismic activity. Hence deformed serpentinite, and possibly blueschist, may facilitate the propagation of

rupture near the plate interface down to depths of 60-80 km, as observed for large shocks (e. g. Tohoku-oki 3/2011, Sumatra 12/2004) and aftershocks (Lay et al., 2012).

Chlorite schists do not show significant porosity variation with deformation, and their low porosity makes the metasomatic plate interface a likely barrier for fluid migration. Low permeability layers at the interface hamper massive upward migration of the aqueous fluids produced by dehydration the subducted crust and limit the serpentinization of the mantle wedge (Fig. 8). The thin layer acting as a seal is expected to break up during large earthquakes, which would allow transient fluid migration from the subducted crust into the forearc mantle wedge and local serpentinization (Fig. 8). Mantle wedge porosity and permeability are expected to vary with the deformation of serpentinites (Fig. 7), especially near the deforming interface where it should increase.

Observations of low-velocity layers in subducted crust suggest that the oceanic crust is over-pressurized down to a depth of 35 - 40 km in hot subduction zones (Audet et al., 2009; Peacock et al., 2011) and 90 km in cold subduction zone (Shiina et al., 2013). The porosity of the subducted oceanic crust deduced from seismic-wave velocities is in the range 1 - 4×10^{-2} (Peacock et al., 2011; Shiina et al., 2013), in agreement with the value of up to 2.6×10^{-2} obtained in the present experiments on blueschists.

Over-pressure in subducted crust requires the presence of a low permeability seal (10^{-24} - 10^{-21} m^2) at the plate interface (Audet et al., 2009; Peacock et al., 2011). According to these authors, such a seal forms by grain-size reduction during shearing or by precipitation of platy minerals such as clay, serpentine or micas. Permeabilities inferred for the sealed subduction interface are similar to those assessed here both for chlorite-schist ($k\approx10^{-24}$ - $10^{-21.5}$ m^2) and undeformed serpentinite ($k\approx10^{-24}$ - $10^{-20.5}$ m^2; Fig. 7). Serpentinite is likely deformed near the subduction interface, hence its porosity would be too high to seal the interface, unless sealing by pressure-solution occurs at timescales larger than those of the

present experiments. We infer that the seal may correspond to a one to several meter-thick chlorite-rich layer presents down to around 45 km in hot subduction zones (such as Cascadia) and down to 90 km in cold ones (such as NE Japan, Fig. 8), consistent with the predicted stability limits of chlorite along the subduction interface for the two different thermal regimes (Abers et al., 2013). Chlorite-schist layers are commonly observed in ophiolites at the metasomatic contact between serpentinites and metamorphosed oceanic crust (Spandler et al., 2008). Pelitic metasediments and metasomatic talc-schists are lithologies with weak phyllosilicates behaving like chlorite that could also contribute to seal the subduction interface.

The presence of a low permeability seal at the interface down to about 80 km in the cold Tohoku subduction zone accounts for three additional seismological observations. Firstly, the high seismic velocities observed in the forearc mantle indicate limited serpentinization and effective plate sealing (Abers et al., 2017). Secondly, release of fluids to the mantle wedge is detected below this depth (Kawakatsu and Watada, 2007). Thirdly, updip fluid migration from the blueschist-eclogite dehydration transition in the oceanic crust can account for high seismicity in the shallower blueschist facies conditions (Kita et al., 2006). Updip fluid migration and overpressured crust may favor the occurrence of large aseismic slip preceding the magnitude 9.0 Tohoku-oki earthquake (Kato et al., 2012).

In young and hot subduction zones such as Cascadia or Shikoku, the presence of thicker metasomatic zones with low-porosity chlorite-type phyllosilicates at depths around 30 to 40 km may favor the occurrence and observation of tremors (Ide, 2012). The high seismic velocities observed worldwide in the forearc mantle of subduction zones hint at limited serpentinization and effective plate sealing, with the two notable exceptions of Cascadia and Costa Rica (Abers et al., 2017). This is an indication of intense fluid flow through the interface of Cascadia, in apparent contradiction with thicker seal than in cold subduction

zone. The large fluid production in hot Cascadia may efficiently break the seal, leading to complex zonation of the mechanical behavior of the interface (Audet and Schaeffer, 2018) and serpentinization of the mantle wedge. In any case, the present determinations of porosities and permeabilities provide experimental values for the essential parameters of mechanical and geodynamical models describing fluid flow in dipping lithologic layers of subduction zones (Morishige and van Keken, 2018).

Acknowledgments

The large volume high-pressure experiments were performed at the PLECE Platform of the Université de Lyon with the help of Sylvie Le Floch. Hervé Cardon and Damien Mollex helped for sample preparation. Gilles Montagnac helped for the Raman spectroscopy. This work was supported by INSU through the national Raman facility in Lyon and "Programme national de Planétologie". We thank Jannick Ingrin for performing the D2-glaucophane isotopic exchange experiments in Lille. This work was supported by grants to BR through the PNP-INSU program, and through LABEX Lyon Institute of Origins (ANR-10-LABX-0066) of the Université de Lyon within the program "Investissements d'Avenir" (ANR-11-IDEX-0007) of the French government operated by the National Research Agency (ANR).

References

Abers, G., Nakajima, J., van Keken, P., Kita, S., Hacker, B., 2013. Thermal-petrological controls on the location of earthquakes within subducting plates. Earth and Planetary Science Letters, 369-370: 178-187.

Abers, G.A., van Keken, P.E., Hacker, B.R., 2017. The cold and relatively dry nature of mantle forearcs in subduction zones. Nature Geoscience, 10: 333.

Amiguet, E. et al., 2012. Creep of phyllosilicates at the onset of plate tectonics. Earth and Planetary Science Letters, 345-348: 142-150.

Amiguet, E., Van de Moortele, B., Cordier, P., Hilairet, N., Reynard, B., 2014. Deformation mechanisms and rheology of serpentines in experiments and in nature. Journal of Geophysical Research-Solid Earth, 119: 4640-4655.

Audet, P., Bostock, M.G., Christensen, N.I., Peacock, S.M., 2009. Seismic evidence for overpressured subducted oceanic crust and megathrust fault sealing. Nature, 457: 76-78.
Audet, P., Schaeffer, A.J., 2018. Fluid pressure and shear zone development over the locked to slow slip region in Cascadia. Science Advances, 4: eaar2982.
Bezacier, L., Reynard, B., Bass, J.D., Sanchez-Valle, C., Van de Moortele, B.V., 2010. Elasticity of antigorite, seismic detection of serpentinites, and anisotropy in subduction zones. Earth and Planetary Science Letters, 289: 198-208.
Chester, F.M. et al., 2013. Structure and Composition of the Plate-Boundary Slip Zone for the 2011 Tohoku-Oki Earthquake. Science, 342: 1208.
Cranck, J., 1975. The mathematics of diffusion. Oxford University Press, Oxford.
Fagereng, Å., den Hartog, S.A.M., 2016. Subduction megathrust creep governed by pressure solution and frictional–viscous flow. Nature Geoscience, 10: 51.
Fulton, P.M. et al., 2013. Low coseismic friction on the Tohoku-Oki fault determined from temperature measurements. Science, 343: 1214-1217.
Ganzhorn, A.-C. et al., 2018. Deuterium□hydrogen inter-diffusion in chlorite. Chemical Geology.
Hilairet, N. et al., 2007. High-pressure creep of serpentine, interseismic deformation, and initiation of subduction. Science, 318: 1910-1913.
Hiraga, T., Anderson, I.M., Kohlstedt, D.L., 2004. Grain boundaries as reservoirs of incompatible elements in the Earth's mantle. Nature, 427: 699.
Ide, S., 2012. Variety and spatial heterogeneity of tectonic tremor worldwide. Journal of Geophysical Research: Solid Earth, 117.
Ingebritsen, S.E., Manning, C.E., 1999. Geological implications of a permeability-depth curve for the continental crust. Geology, 27: 1107-1110.
Ingebritsen, S.E., Manning, C.E., 2010. Permeability of the continental crust: dynamic variations inferred from seismicity and metamorphism. Geofluids, 10: 193-205.
Katayama, I., Terada, T., Okazaki, K., Takinawa, W., 2012. Episodic tremor and slow slip potentially linked to permeability contrasts at the Moho. Nature Geoscience, Advance online publication.
Kato, A. et al., 2012. Propagation of Slow Slip Leading Up to the 2011 M_w 9.0 Tohoku-Oki Earthquake. Science, 335: 705.
Kawakatsu, H., Watada, S., 2007. Seismic evidence for deep-water transportation in the mantle. Science, 316: 1468-1471.
Kawano, S., Katayama, I., Okazaki, K., 2011. Permeability anisotropy of serpentinite and fluid pathways in a subduction zone. Geology, 39: 939-942.
Khoshmanesh, M., Shirzai, M., 2018. Episodic creep events on the San Andreas Fault caused by pore pressure variations. Nature Geoscience, 11: 610-614.
Kita, S., Okada, T., Nakajima, J., Matsuzawa, T., Hasegawa, A., 2006. Existence of a seismic belt in the upper plane of the double seismic zone extending in the along-arc direction at depths of 70-100 km beneath NE Japan. Geophysical Research Letters, 33: L24310.
Ko, B., Jung, H., 2015. Crystal preferred orientation of an amphibole experimentally deformed by simple shear. Nature Communications, 6: 6586.
Koga, K.T., Daniel, I., Reynard, B., 2005. Determination of trace element partition coefficients between water and minerals by high-pressure and high-temperature experiments: Leaching technique. Geochemistry Geophysics Geosystems, 6: 10.1029/2005GC000944.
Kronenberg, A.K., Kirby, S.H., Pinkston, J., 1990. Basal slip and mechanical anisotropy of biotite. Journal of Geophysical Research-Solid Earth and Planets, 95: 19257-19278.

Lay, T. et al., 2012. Depth-varying rupture properties of subduction zone megathrust faults. Journal of Geophysical Research: Solid Earth, 117.
Mibe, K., Fujii, T., Yasuda, A., 1999. Control of the location of the volcanic front in island arcs by aqueous fluid connectivity in the mantle wedge. Nature, 401: 259-262.
Morishige, M., van Keken, P.E., 2018. Fluid migration in a subductiong viscoelastic slab. Geochemistry, Geophysics, Geosystems, 19: 337-355.
Peacock, S.M., Christensen, N.I., Bostock, M.G., Audet, P., 2011. High pore pressures and porosity at 35 km depth in the Cascadia subduction zone. Geology, 39: 471-474.
Pezzotti, G., Kleebe, H.J., Ota, K., T., N., 1997. Viscoelastic sliding and diffusive relaxation along grain boundaries in polycrystalline boron nitride. Acta Materialia, 45: 4171-4179.
Pilorgé, H. et al., 2017. D/H diffusion in serpentine. Geochimica et Cosmochimica Acta, 211: 355-372.
Reynard, B., Caracas, R., 2009. D/H isotopic fractionation between brucite $Mg(OH)_2$ and water from first-principles vibrational modeling. Chemical Geology, 262: 159-168.
Reynard, B., Mibe, K., Van de Moortele, B., 2011. Electrical conductivity of the serpentinised mantle and fluid flow in subduction zones. Earth and Planetary Science Letters, 307: 387-394.
Sanford, W.E., 2017. Estimating regional-scale permeability–depth relations in a fractured-rock terrain using groundwater-flow model calibration. Hydrogeology Journal, 25: 405-419.
Schwartz, S. et al., 2013. Pressure-temperature estimates of the lizardite/antigorite transition in high pressure serpentinites. Lithos, 178: 197-210.
Shiina, T., Nakajima, J., Matsuzawa, T., 2013. Seismic evidence for high pore pressures in the oceanic crust: Implications for fluid-related embrittlement. Geophysical Research Letters, 40: 2006-2010.
Shmonov, V.M., Vitiovtova, V.M., Zharikov, A.V., Grafchikov, A.A., 2003. Permeability of the continental crust: implications of experimental data. Journal of Geochemical Exploration, 78-79: 697-699.
Shmonov, V.M., Vitovtova, V.M., Zarubina, I.V., 1995. Permeability of rocks at elevated temperatures and pressures. In: Shmulovich, K.I., Yardley, B.W.D., Gonchar, G.G. (Eds.), Fluids in the Crust: Equilibrium and transport properties. Springer Netherlands, Dordrecht, pp. 285-313.
Sleep, N.H., Blanpied, M.L., 1992. Creep, compaction, and the weak rheology of major faults. Nature, 359: 687-692.
Spandler, C., Hermann, J., Faure, K., Mavrogenes, J.A., Arculus, R.J., 2008. The importance of talc and chlorite “hybrid” rocks for volatile recycling through subduction zones; evidence from the high-pressure subduction mélange of New Caledonia. Contributions to Mineralogy and Petrology, 155: 181-198.
Syracuse, E.M., van Keken, P.E., Abers, G.A., 2010. The global range of subduction zone thermal models. Physics of the Earth and Planetary Interiors, 183: 73-90.
Ujiie, K. et al., 2013. Low Coseismic Shear Stress on the Tohoku-Oki Megathrust Determined from Laboratory Experiments. Science, 342: 1211.
Wada, I., Wang, K.L., He, J.G., Hyndman, R.D., 2008. Weakening of the subduction interface and its effects on surface heat flow, slab dehydration, and mantle wedge serpentinization. Journal of Geophysical Research-Solid Earth, 113.
Walder, J., Nur, A., 1984. Porosity reduction and crustal pore pressure development. Journal of Geophysical Research, 89: 11,539-11,548.
Wark, D.A., Watson, E.B., 1998. Grain-scale permeabilities of texturally equilibrated, monomineralic rocks. Earth and Planetary Science Letters, 164: 591-605.

Figure captions

Fig. 1. Experimental procedure. a. Cartoon of the experimental procedure. b. Piston displacement (blue), temperature (red) and pressure (green) curves as recorded during the C-25-315 experiment. Step 1: Pressure increase at ambient temperature. Step 2: Increase of temperature at high-pressure. 80-90% of the strain occurs during steps 1 & 2 (blue dashed line for C-25-315 and shaded grey area for all experiments), mimicking large strain rates associated with an earthquake. Step 3: Pressure and temperature plateau where deuterium-hydrogen exchange occurs between rock and fluid. Step 4: Piston displacement is only slightly recovered after decompression, demonstrating the large irreversible deformation.

Fig. 2. Isotopic zonation by Raman mapping and texture by SEM of an antigorite sample exchanged with D_2O at 540°C and 3 GPa for 38 hours (redrawn from Pilorgé et al., 2017). a. Raman map of the D/(D+H) ratio, the dashed lines indicate the approximate outline of a large single crystal of antigorite. b. SEM image, ellipses show the approximate location of diffusion zoning observed in a. The two diffusion domains are separated by very fine porosity (green line). c. high magnification SEM image showing nanoporosity that was active during isotopic exchange at high temperature. In the opposite, cracks visible in b. that cross-cut the isotopic zonation (red lines) were created after quenching, most likely during decompression.

Fig. 3. Determination of the grain boundary density. a. Initial D/(D+H) data. b. Schematic geometry of one pixel with several new grain boundaries. c. Corresponding schematic diffusion profile. C_1 is the D/(D+H) ratio of the fluid. $C_0 \sim 0$ is the initial ratio in the mineral. l is the half thickness of the plane sheet model used to calculate the diffusion profile. d. Example of synthetic relationship between D/(D+H) and the number of grain boundaries (n) for one pixel of size Y (for conditions of experiment SB-4-315), and the linear fit used. e.

Final map of grain boundary density calculated for SB-4-315. White on the color scale corresponds to discarded spectra for saturated signals.

Fig. 4. BSE images of heterogeneously deformed antigorite laths in experiment SB-4-315. a. Zone of deformed antigorite laths. b. Zoom-in on a deformed area showing numerous parallel cracks forming new grain boundaries. c. Zoom-in on an undeformed area. d. Zoom-in on a deformed area showing fan-shaped cracks. e. Corresponding D/(D+H) map from Fig. 3.

Fig. 5. D/(D+H) and grain boundary density maps (first and second image, respectively) for blueschist G (a), deformed serpentinite SB (b, P1: almost undeformed zone; P2: highly deformed zone), undeformed serpentinite SC (c), and the chlorite schist C (d). The grain boundary density and D/(D+H) color scales are the same for all maps. White pixels are discarded from analysis due to low signal/noise ratio. (e) Histograms corresponding to grain boundary maps for the four experiments. Red dashed line: mean density used to calculate porosity.

Fig. 6. Maps of grain boundary density at the capsule scale. Dashed lines: cores contours. The color scale is the same as in Fig. 5. a. blueschist (G-28-500). White arrow indicates a band of higher porosity zone in the blueschist chip. Porosity is the highest in the powder. b. serpentinite (SB-4-315). Serpentinite chip shows heterogeneities due to localized deformation. Powder appears dark due to low signal associated with poorly polished surface. Location of high-resolution maps in Fig. 5 is shown.

628 Fig. 7. a) Permeability-porosity diagram, with present porosity data in blue: blueschist; dark
629 green: chlorite schist; medium green: antigorite serpentinite SC; light green: deformed
630 antigorite serpentinite SB. Dashed arrows: trend low-pressure data for gabbro (orange) and
631 serpentinite (green), respectively, define a Kozeny-Carman relationship with typical exponent
632 n=2 (Katayama et al., 2012; Kawano et al., 2011) used to estimate permeabilities from the
633 present porosity determinations. Permeabilities of the different rocks are slightly offset for
634 readability. Red: high-pressure data on textural equilibrium experiments on quartzite with
635 typical exponent n=3 (Wark and Watson, 1998). Grey area: impermeable rock domain. b)
636 Comparison of estimated permeabilities in a) with those based on hydraulic and heat flow
637 measurements in stable continental crust (Ingebritsen and Manning, 1999), solid and long-
638 dashed black lines, after earthquakes (Ingebritsen and Manning, 2010), grey lines, and
639 measurements on deep core rocks (Shmonov et al., 2003), short-dashed black line.
640 Uncertainties are shown as vertical bars on the right of the diagram.
641
642 Fig. 8. Schematic model of water circulation in hot (a) and cold (b) subduction zones taking
643 into account the present porosity and permeability determinations. a. Down to 40 km, the
644 subduction interface corresponds to a low porosity layer (*e.g.* chlorite schists) that act as a
645 seal leading to overpressure within the subducted crust and hampering fluid flow in the
646 mantle corner. Fluids, generated in large quantities especially at the eclogite (E) – blueschist
647 (BS) transition, can penetrate the cold corner of the mantle wedge at greater depths leading to
648 serpentinization of the mantle, as evidenced in the Cascadia subduction zone. b. The
649 subduction interface is sealed down to 80-90 km hampering fluid flow in the mantle corner
650 (seal thickness of a few meters to a few tens of meters is exaggerated). Fluid flows upward
651 within the high porosity blueschist causing earthquakes (Kita et al., 2006) and fluid
652 overpressure (Shiina et al., 2013) in the crust as observed in NE Japan. Fluid flow across the

subduction interface may occur only after earthquake that eventually break the seal, leading to weak localized serpentinization of the mantle corner, or to fluid release to the mantle below 80-90 km depth (Kawakatsu and Watada, 2007). GS: greenschist facies; BS: blueschist facies; E: eclogite facies.

659 Table 1. Experimental conditions for the experiments used for porosity quantification

660 assuming pore width in the range 0.5-2 nanometers and one order of magnitude uncertainty in

661 diffusion coefficients.

Name	Starting material	T (°C)	P (GPa)	Duration (h)	□□□□□□□□ (%)
SB-4-315	Atg (SB)	315	3	12	0.1-1.6
SC-24-315	Atg (SC)	315	1.5	14	0.01-0.6
C-25-315	Chl (SZ24)	315	1.5	14	0.01-0.2
G-28-500	Gl, Ep (G)	500	2.5	14	0.2-2.6
G-31-450	Gl, Ep (G)	450	2.5	48	0.3-2.1

662 Atg: antigorite. Chl: Chlorite. Gl: glaucophane. Ep: Epidote.

663

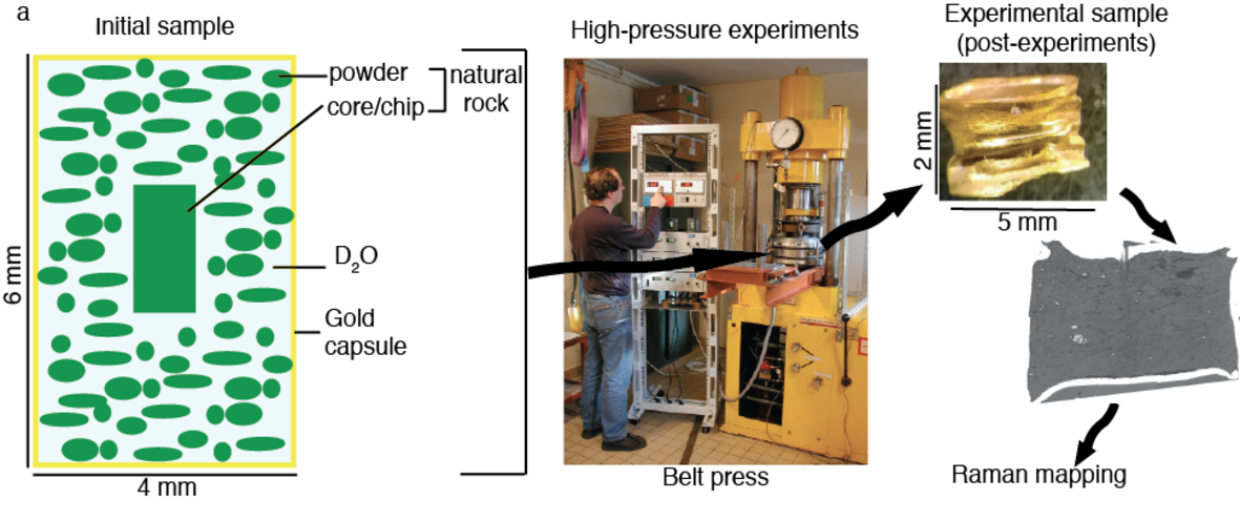
a
Initial sample
powder
core/chip
natural rock
D2O
Gold capsule
6 mm
4 mm
High-pressure experiments
Belt press
Experimental sample (post-experiments)
2 mm
5 mm
Raman mapping

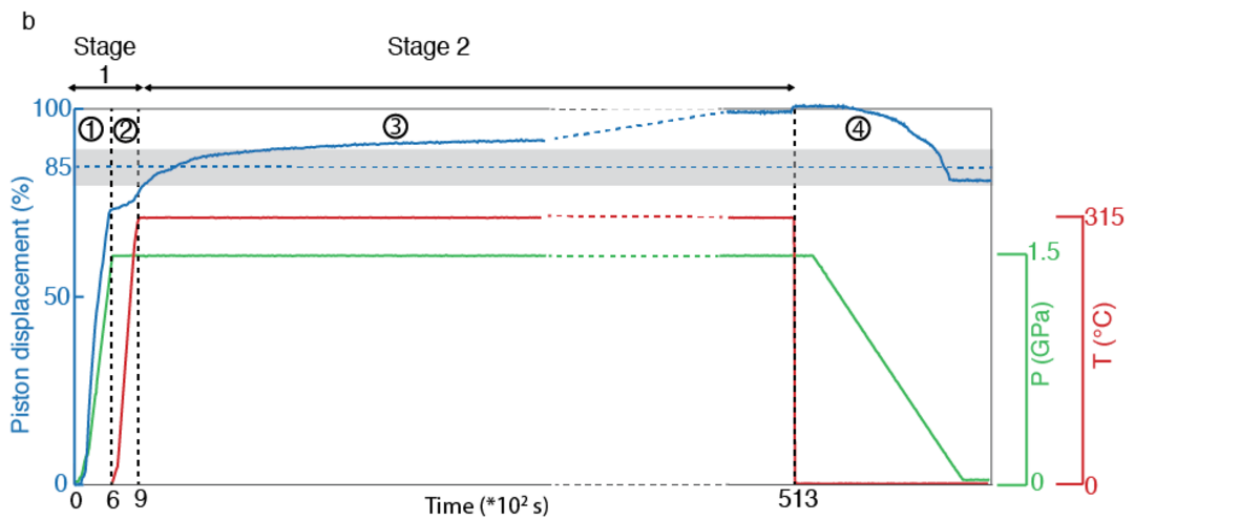
b
Stage 1
Stage 2
①
②
③
④
100
85
50
0
Piston displacement (%)
0
6
9
513
Time (*10² s)
1.5
0
P (GPa)
315
0
T (°C)

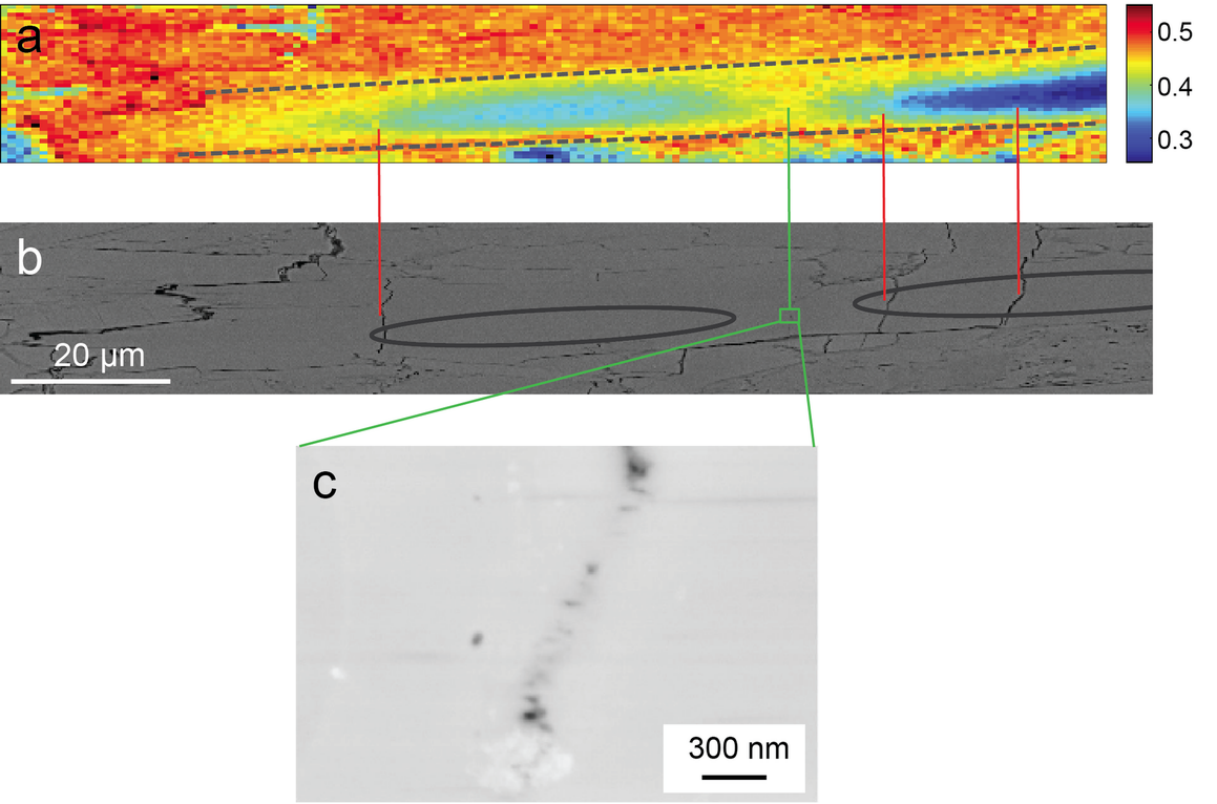
a
0.5
0.4
0.3
b
20 µm
c
300 nm

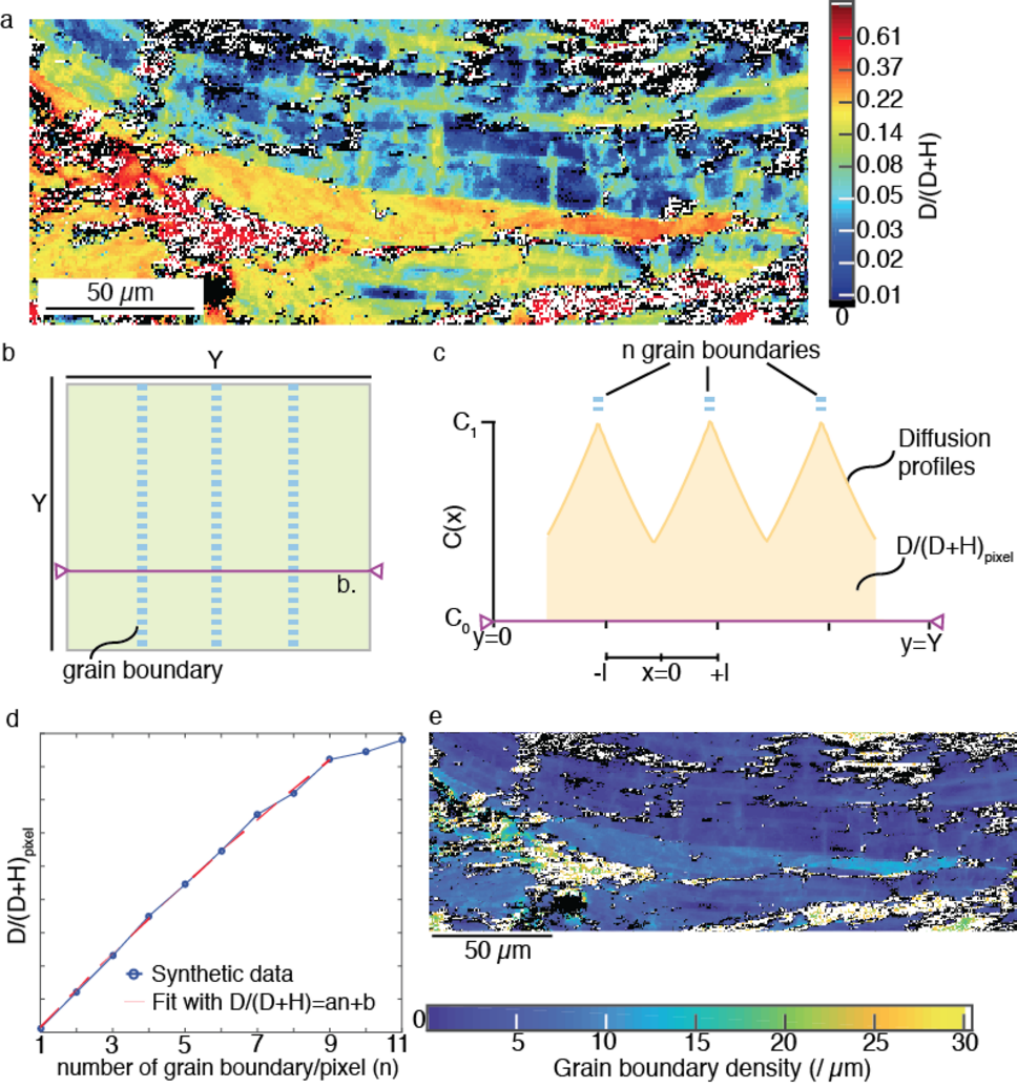
a
0.61
0.37
0.22
0.14
0.08
0.05
0.03
0.02
0.01
0
D/(D+H)
50 μm
b
Y
Y
b.
grain boundary
c
n grain boundaries
C1
C(x)
C0
Diffusion profiles
D/(D+H)pixel
y=0
y=Y
-l
x=0
+l
d
D/(D+H)pixel
Synthetic data
Fit with D/(D+H)=an+b
1
3
5
7
9
11
number of grain boundary/pixel (n)
e
50 μm
0
5
10
15
20
25
30
Grain boundary density (/ μm)

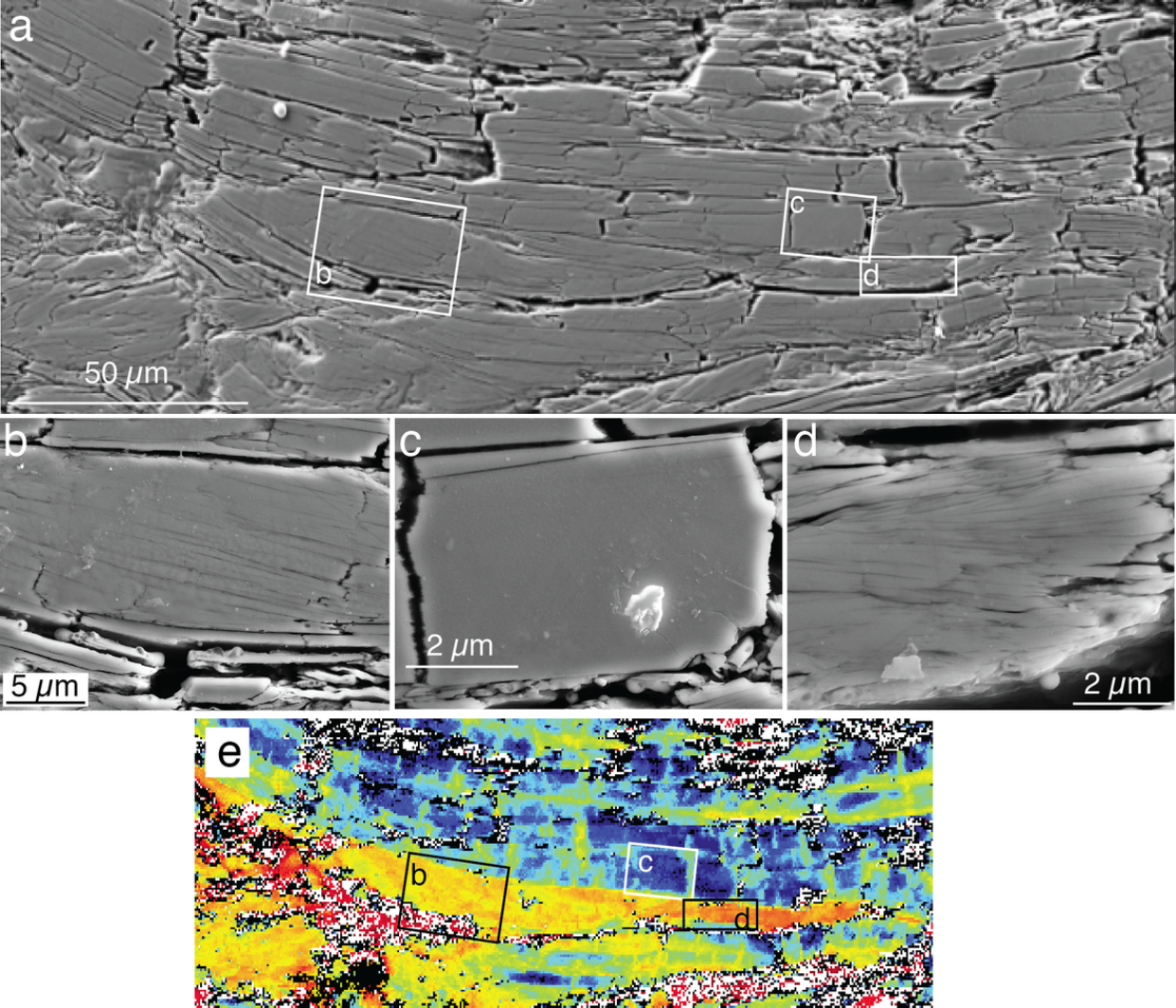
a
b
c
d
50 μm
b
5 μm
c
2 μm
d
2 μm
e
b
c
d

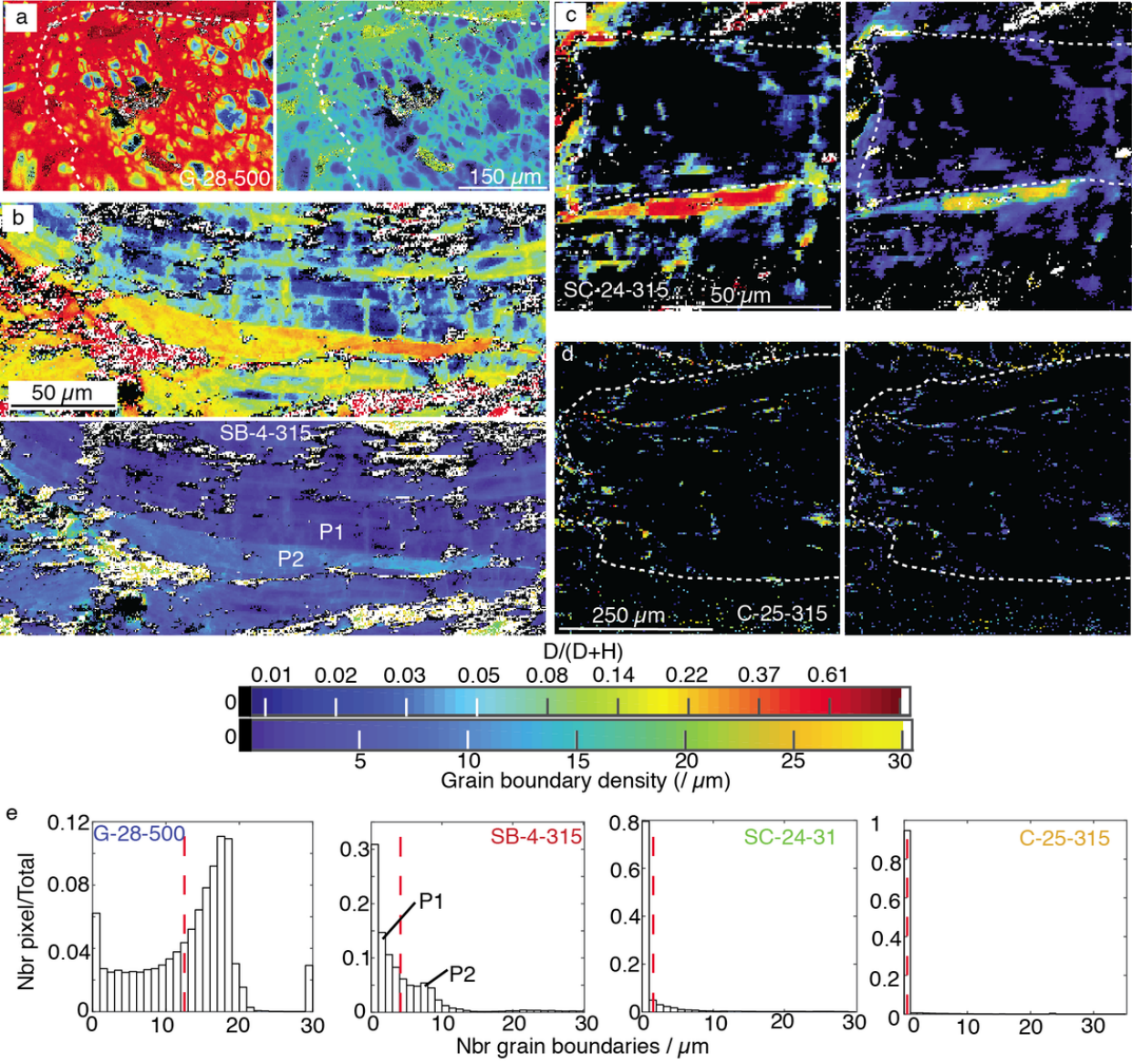
a
G-28-500
150 μm
b
50 μm
SB-4-315
P1
P2
c
SC-24-315
50 μm
d
250 μm
C-25-315
D/(D+H)
0.01 0.02 0.03 0.05 0.08 0.14 0.22 0.37 0.61
0
0
5 10 15 20 25 30
Grain boundary density (/ μm)
e
G-28-500
SB-4-315
SC-24-31
C-25-315
P1
P2
Nbr pixel/Total
Nbr grain boundaries / μm

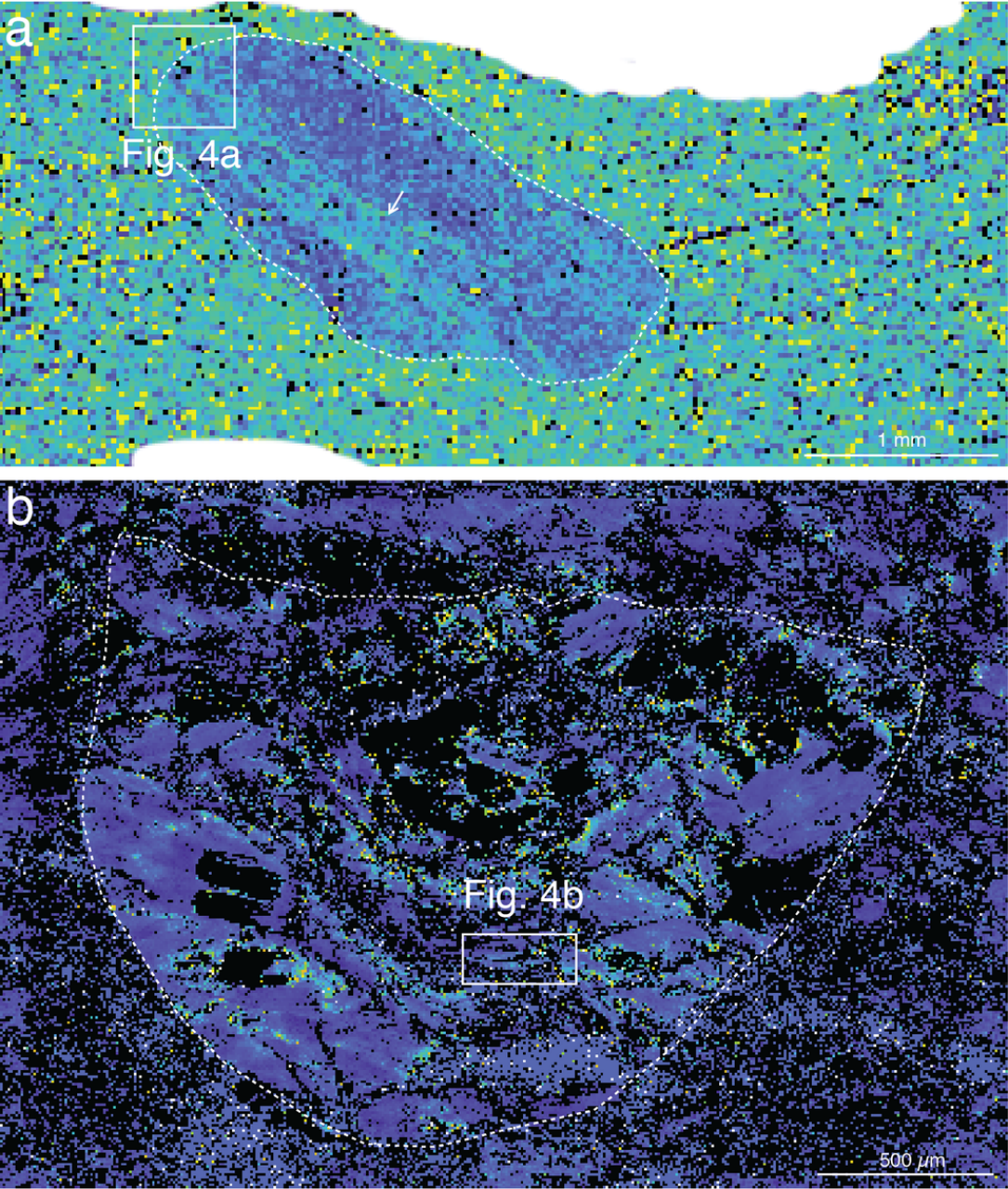
a
Fig. 4a
1 mm
b
Fig. 4b
500 μm

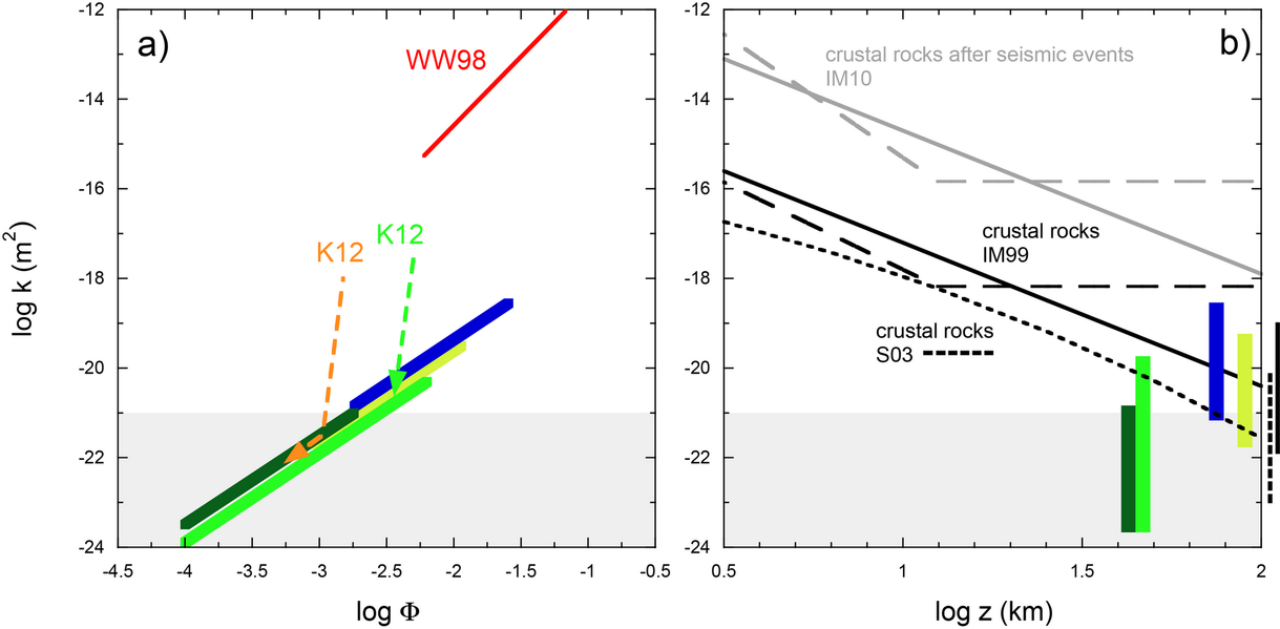
a)
b)
WW98
K12
K12
crustal rocks after seismic events
IM10
crustal rocks
IM99
crustal rocks
S03
log k (m²)
log Φ
log z (km)
-12
-14
-16
-18
-20
-22
-24
-4.5
-4
-3.5
-3
-2.5
-2
-1.5
-1
-0.5
0.5
1
1.5
2

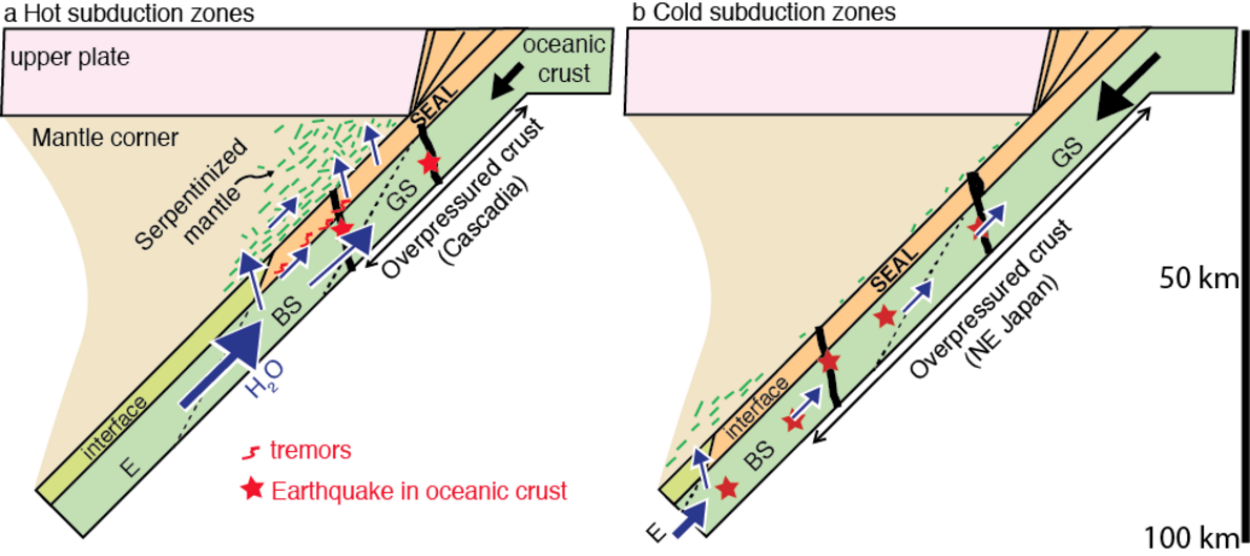
a Hot subduction zones
upper plate
oceanic crust
Mantle corner
Serpentinized mantle
SEAL
GS
Overpressured crust (Cascadia)
BS
H_2O
interface
E
tremors
Earthquake in oceanic crust
b Cold subduction zones
GS
SEAL
Overpressured crust (NE Japan)
50 km
interface
BS
E
100 km